
MOREPHY-NET: AN EVOLUTIONARY MULTI-OBJECTIVE OPTIMIZATION FOR REPLICA-EXCHANGE-BASED PHYSICS-INFORMED OPERATOR LEARNING NETWORK

Binghang Lu

School of Electrical and Computer Engineering
Purdue University
610 Purdue Mall, West Lafayette, IN 47907
lu895@purdue.edu

Changhong Mou

Department of Mathematics and Statistics
Utah State University
3900 Old Main Hill, Logan, UT 84322
changhong.mou@usu.edu

Guang Lin

Department of Mathematics and School of Mechanical Engineering
Purdue University
610 Purdue Mall, West Lafayette, IN 47907
guanglin@purdue.edu

February 18, 2026

ABSTRACT

In this paper, we propose an evolutionary **Multi-objective Optimization for Replica-Exchange-based Physics-informed Operator learning Network** (Morephy-Net), which is a novel operator learning network to efficiently solve parametric partial differential equations that requires only a minimal amount of noisy observational data in both forward and inverse settings. While physics-informed neural networks and operator learning approaches such as Deep Operator Networks and Fourier Neural Operators offer promising alternatives to traditional numerical solvers, they struggle with balancing operator and physics losses, maintaining robustness under noisy or sparse data, and providing uncertainty quantification. The proposed framework addresses these limitations by integrating: (i) evolutionary multi-objective optimization to adaptively balance operator and physics-based losses in the Pareto front; (ii) replica exchange stochastic gradient Langevin dynamics to improve global parameter-space exploration and accelerate convergence; and (iii) built-in Bayesian uncertainty quantification from stochastic sampling. The proposed operator learning method is tested numerically on several different problems including one-dimensional Burgers equation and the time-fractional mixed diffusion-wave equation. The results indicate that our framework consistently outperforms the general operator learning methods in accuracy, noise robustness, and the ability to quantify uncertainty.

1 Introduction

The accurate and efficient solution of partial differential equations (PDEs) is indispensable in modeling and understanding a wide range of physical, biological, and engineering systems [1, 2, 3]. Solving parametric PDEs with varying geometries, parameters, and initial/boundary conditions is equivalent to learning the solution operator that maps inputs to their corresponding solutions [4, 5, 6]. For complex systems, traditional methods such as the finite difference method (FDM) and finite element method (FEM) often require prohibitive computational resources as they need fine spatial-temporal discretization and repeated simulations for different parameters and initial/boundary conditions [7, 8, 9, 10, 5]. In recent years, machine learning (ML) has become a powerful and increasingly popular alternative to traditional numerical solvers for parametric PDEs [11, 12, 13, 14, 15, 16, 17, 18]. There are several different ML approaches for solving PDEs. Among them, one prominent category is *physics-informed neural networks (PINNs)*

[19], which incorporate the underlying physical laws directly into the training process. PINNs have shown success in approximating solutions to specific PDE instances and extending them to learn solution operators that generalize across varying inputs, i.e., parametric PDEs has attracted growing interest. However, training PINNs for parametric PDEs remains computationally expensive, particularly in multi-query or real-time scenarios, and this setting often requires overly complex parameterizations [20, 21]. Another alternative is *operator learning*, such as the Deep Operator Network (DeepONet or DON) [13] and Fourier Neural Operator (FNO) [22], which aim to directly learn the mapping from input functions to PDE solutions. However, their performance often deteriorates in challenging settings, including inverse problems, noisy or sparse observational data, and high-dimensional parameter spaces [23].

To address the limitations of traditional operator learning, Wang et al. [24] proposed a physics-informed DeepONet framework for parametric PDEs that combines the operator-learning capability of DeepONets with PDE residual constraints, as in PINNs. This framework reduces the dependence of general operator learning on large amounts of paired high-resolution training data and preserves consistency to the original PDEs with different discretizations. In particular, physics-informed DeepONets adopt a composite loss function consisting of: (1) an operator loss, and (2) a physics loss derived from the PDE residual. [24] showed that physics-informed DeepONets are data-efficient and particularly effective in small-data regimes. Nevertheless, several challenges inherent to the physics-informed DeepONets framework persist. First, similar to PINNs, the training of physics-informed DeepONets admits a multi-objective optimization problem, where the operator loss and the physics loss from the PDE residual must be balanced appropriately [25, 26]. Second, in real applications, the available data are often contaminated with noise. Such noise can diminish the accuracy of the learned operator and even destabilize the training process, particularly in inverse problem settings where the physics loss alone may be insufficient to adequately regularize the solution [23, 27]. Third, since operator learning optimization often relies on gradient-based methods such as the Adam optimizer, the current physics-informed DeepONet framework lacks the ability for uncertainty quantification [28, 29].

To address the aforementioned challenges for operator learning in PDEs, we propose the new *Multi-Objective Replica Exchange Physics Informed Neural Operator Network* (Morephy-Net). The Morephy-Net extends the physics informed operator learning framework with the following key components: (i) an evolutionary multi-objective optimization algorithm to balance operator loss and physics loss, thereby improving both accuracy and convergence; (ii) a replica exchange stochastic gradient Langevin dynamics (reSGLD) is used as effective sampler to facilitate global parameter-space exploration and mitigate entrapment in poor local minima; and (iii) integrated uncertainty quantification (UQ) to assess prediction confidence and robustness in both forward and inverse problems settings. More specifically, Morephy-Net employs the modified version of reference-point-based non-dominated sorting approach (hereafter referred to as refined NSGA-III) [30], improved for operator learning in this work with the proposed refined Pareto sampling (RPS) strategy. With RPS that enrich the sampling diversity in the Pareto front, the proposed refined NSGA-III treats each loss function as a distinct objective and during training, non-dominated sorting and crowding distance calculations are used to identify solutions along the optimal Pareto front where each objectives are balanced. The reSGLD used in Morephy-Net is to improve parameter-space exploration during training. Indeed, the standard stochastic gradient Langevin dynamics (SGLD) [31] augments stochastic gradient descent with Gaussian noise that provides the approximation of posterior sampling while optimizing the model. In high-dimensional, non-convex landscapes, however, the standard SGLD can become trapped in local minima. In such case, reSGLD [32, 33, 34] runs multiple SGLD processes at different temperatures and periodically exchanges their states which takes the advantages that high-temperature chains explore broader regions of the energy landscape, facilitating escape from local traps, while low-temperature chains focus on fine-tuning around promising optima. Thus, the mechanism enables Morephy-Net to achieve fast convergence, deliver reliable parameter estimates, and quantify uncertainty for both forward and inverse PDE problems. We summarize the main contribution to this work as follows:

1. The Morephy-Net involves the *evolutionary multi-objective optimization* in the physics informed operator learning framework via the NSGA-III algorithm which treats the data loss and physics loss as distinctive objectives and effectively addresses the challenge of balancing the weight for each loss term.
2. A refined Pareto sampling (RPS) strategy is proposed in NSGA-III algorithm which improves the diversity of sampling by re-selecting distinctive solutions along the Pareto front and mitigates clustering in local regions.
3. The *replica exchange stochastic gradient Langevin dynamics (reSGLD)* is used to improve the global parameter space exploration, where high-temperature chains traverse broader regions of the energy landscape to escape local minima and low-temperature chains refine solutions that can accelerate the convergence and improving the accuracy.
4. The inherent reSGLD also allows the *uncertainty quantification (UQ)* for the operator learning framework in both forward and inverse PDE problem settings.

The remainder of this paper is organized as follows: Section 2 describes the proposed Morephy-Net framework in detail that includes its main components: physics-informed DeepONet (Section 2.2), NSGA-III multi-objective optimization

(Section 2.3), Replica Exchange Stochastic gradient Langevin dynamics (Section 2.4), and its uncertainty quantification (Section 2.5). Section 3 presents numerical experiments on different test problems. Finally, Section 4 concludes the paper and discusses potential future directions.

2 General framework

2.1 Overview

The Physics-Informed Multi-Objective Refined Fourier Deep Operator Network (PIMORE-FDON) framework consists of several key components, as illustrated schematically in Figure 2. In particular, PIMORE-FDON consist the following: (1) **Physics-informed Deep Operator Network (PI-DON) architecture.** The Deep Operator Network employs two subnetworks—the branch network that includes the initial conditions or PDE parameters, and the trunk network, which may contain the spatial temporal grid information. The training is guided not only by data loss but also by a physics-informed residual loss that enforces the governing PDE constraints (see Section 2.2). (2) **Fourier convolution layer.** The Fourier convolution layer maps the latent representation into a spectral space, where the underlying information can be more effectively represented by the neural network. This transformation also allows the model to capture global dependency and long-range interactions inherently in data. (3) **Multi-objective optimization with replica exchange stochastic gradient Langevin dynamics.** In PIMORE-FDON, the training process integrates the refined Non-dominated Sorting Genetic Algorithm III (refined NSGA-III) algorithm (see Section 2.3), proposed in this paper, with replica exchange stochastic gradient Langevin dynamics (reSGLD) (see Section 2.4) to address the challenges of multi-objective optimization in physics-informed operator learning. The refined NSGA-III serves as the evolutionary mechanism for exploring the Pareto front that produces optimal candidate solutions. These candidates are then further optimized through reSGLD, which improves exploration of the parameter space by including stochastic gradient noise and enabling replica exchanges across parallel chains at different “temperatures.” This stochastic strategy not only helps the models escape local minima but also improves convergence in training.

Morephy-Net: Evolutionary Multi-objective Physics-informed Operator Learning with Replica Exchange & UQ for Parametric PDEs

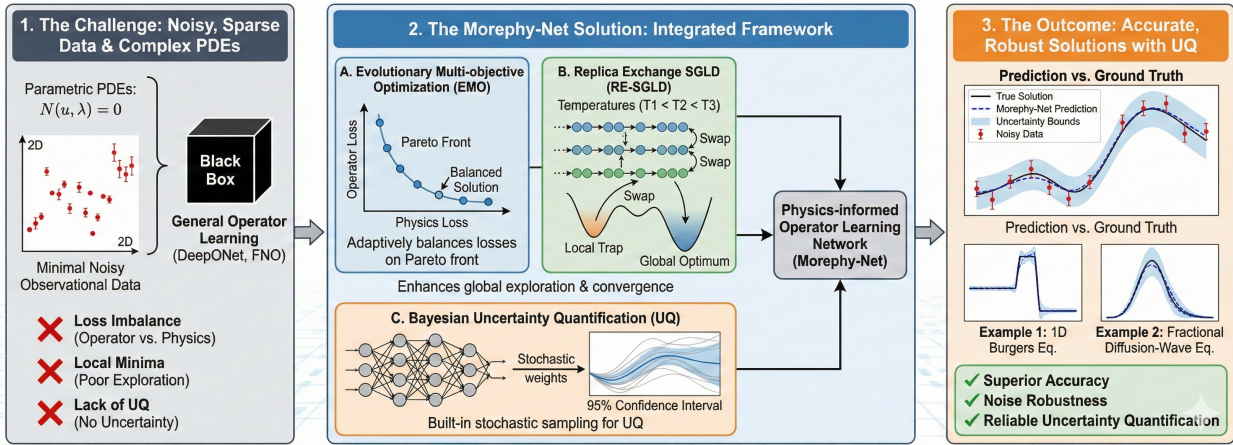


Figure 1: The diagram of Morephy-Net. The framework integrates three key components: (A) Evolutionary Multi-objective Optimization (EMO), (B) Replica Exchange Stochastic Gradient Langevin Dynamics (RE-SGLD), (C) Bayesian Uncertainty Quantification (UQ)

Figure 1 outlines the Morephy-Net approach for addressing the challenges of learning operator solutions from noisy, sparse data. The framework overcomes limitations of conventional methods (such as loss imbalance and poor exploration) by integrating three key components: (A) Evolutionary Multi-objective Optimization (EMO) to adaptively balance operator and physics losses along a Pareto front; (B) Replica Exchange Stochastic Gradient Langevin Dynamics (RE-SGLD) to escape local minima and improve global exploration; and (C) Bayesian Uncertainty Quantification (UQ) via stochastic sampling. The outcome, demonstrated on benchmark problems like the 1D Burgers and fractional diffusion-wave equations, is a robust operator learning network that provides superior accuracy, noise resilience, and reliable uncertainty estimates.

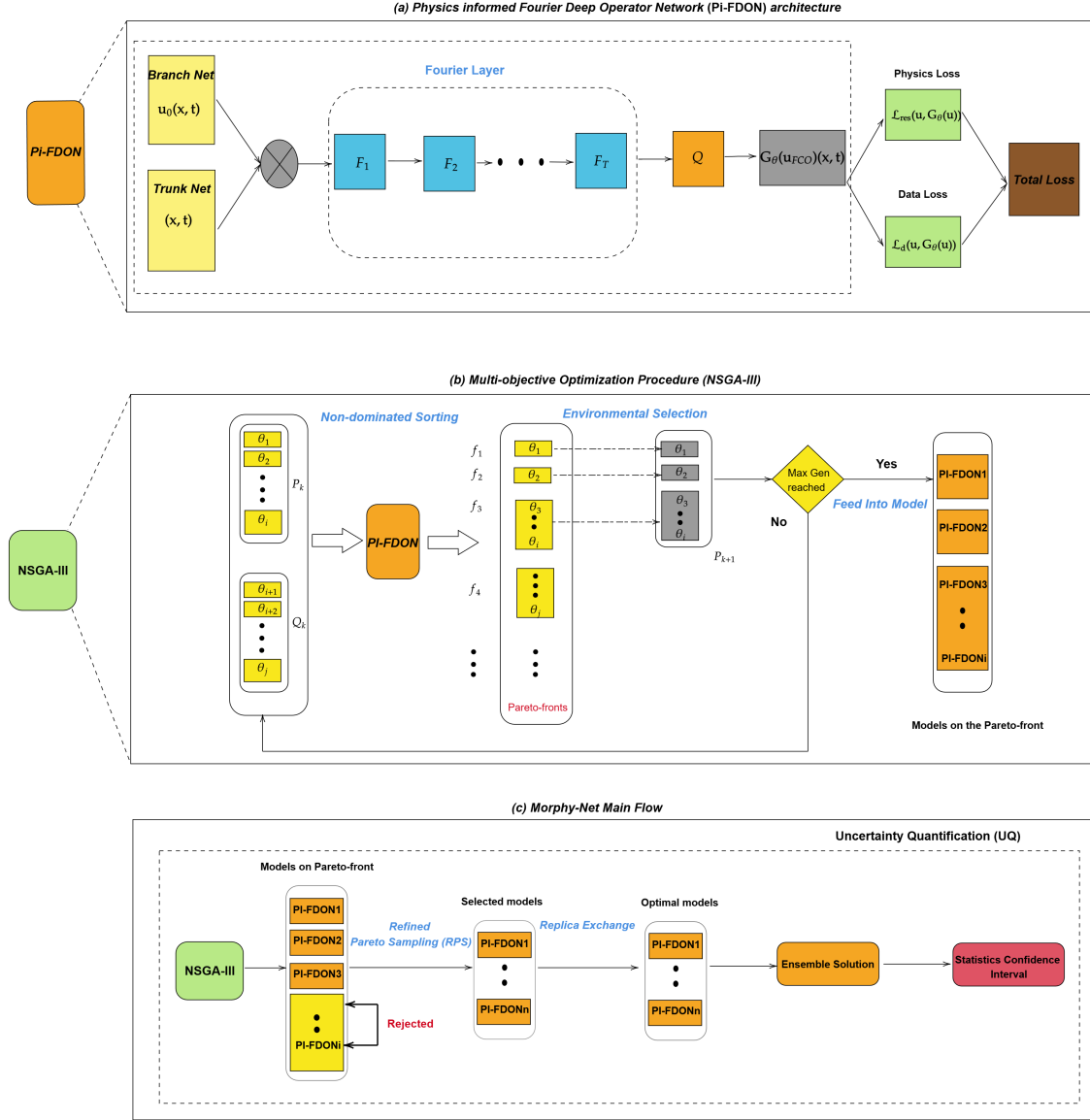


Figure 2: Schematic illustration of Morephy-Net framework. Top panel (a): The Physics-informed Deep Operator Network (PI-DON) architecture consists of branch and trunk subnetworks that encode PDE parameters/initial conditions and spatio-temporal inputs, respectively. Training is guided by both data loss and physics-informed residual loss, with a Fourier layer applied after the dot product of the branch and trunk networks. Middle panel (b) Multi-objective optimization with the refined Non-dominated Sorting Genetic Algorithm III (refined NSGA-III). Bottom panel (c). Replica exchange stochastic gradient Langevin dynamics (reSGLD) used for uncertainty quantification.

2.2 Physics Informed Deep Operator Network

The general deep operator network (DeepONet) proposed [13] with mathematical foundation of the universal operator approximation theorem [35] is intended to learn nonlinear operator mappings between infinite-dimensional function spaces. For a general PDE problem, we introduce the solution operator

$$\mathcal{G}(\kappa) = u(\cdot; \kappa), \tag{1}$$

where κ represents the input which can be the initial condition or parameters of the PDE. A DeepONet is usually a class of neural network models designed to approximate \mathcal{G} . In particular, we denote by G_θ the DeepONet approximation of \mathcal{G} ,

with θ representing the trainable parameters of the network. Then a DeepONet usually consists of two subnetworks: the branch net and the trunk net and the estimator evaluated at $\mathbf{x} \in M$ is an inner product of the branch and trunk outputs:

$$G_{\theta}(\kappa(\Xi))(\mathbf{x}) = \sum_{k=1}^p b_k(\kappa(\xi_1), \kappa(\xi_2), \dots, \kappa(\xi_m)) t_k(\mathbf{x}) + b_0, \quad (2)$$

where $b_0 \in \mathbb{R}$ is a bias, $\{b_1, b_2, \dots, b_p\}$ are the p outputs of the branch net, and $\{t_1, t_2, \dots, t_p\}$ are the p outputs of the trunk net. More specifically, the branch network represents κ in a discrete format:

$$\kappa(\Xi) = \{\kappa(\xi_1), \kappa(\xi_2), \dots, \kappa(\xi_m)\}, \quad (3)$$

where $\kappa(\Xi)$ is a vector which consist the evaluation of input functions at different sensors $\Xi = \{\xi_1, \xi_2, \dots, \xi_m\}$. The trunk network may take as input a spatial location $\mathbf{x} \in M$. Our goal is to predict the solution corresponding to a given κ , which is also evaluated at the same input location $\mathbf{x} \in M$. The representation of κ through pointwise evaluations at arbitrary sensor locations provides additional flexibility, both during training and in prediction, particularly when κ is available only through its values at these sensor points.

Given the training data with labels in the two sets of inputs and outputs:

$$\text{input:} \quad \left\{ \kappa^{(k)}, \Xi, (\mathbf{x}_i^{(k)})_{i=1, \dots, N} \right\}_{k=1, \dots, N_{\text{data}}} \quad (4)$$

$$\text{output:} \quad \left\{ u(\mathbf{x}_i^{(k)}; \kappa^{(k)}) \right\}_{i=1, \dots, N, k=1, \dots, N_{\text{data}}}. \quad (5)$$

we minimize a loss function that measures the discrepancy between the true solution operator $G(\kappa^{(k)})$ and its DeepONet approximation $G_{\theta}(\kappa^{(k)})$:

$$\widehat{\mathcal{L}}_{\text{data}}(\theta) = \frac{1}{N_{\text{data}}N} \sum_{k=1}^{N_{\text{data}}} \sum_{i=1}^N \left| G_{\theta}(\kappa^{(k)}(\Xi))(\mathbf{x}_i^{(k)}) - G(\kappa^{(k)})(\mathbf{x}_i^{(k)}) \right|^2, \quad (6)$$

where $X^{(k)} = \{\mathbf{x}_1^{(k)}, \dots, \mathbf{x}_N^{(k)}\}$ denotes the set of N evaluation points in the domain of $G(\kappa^{(k)})$. In practice, however, the analytical solution of the PDE is not available. Instead, we rely on numerical simulation obtained from high fidelity numerical solvers which can be denoted as:

$$\left\{ \hat{u}(\mathbf{x}_i^{(k)}; \kappa^{(k)}) \right\}_{i=1, \dots, N, k=1, \dots, N_{\text{data}}}. \quad (7)$$

Then the practical training tends to minimize the loss function

$$\mathcal{L}_{\text{data}}(\theta) = \frac{1}{N_{\text{data}}N} \sum_{k=1}^{N_{\text{data}}} \sum_{i=1}^N \left| G_{\theta}(\kappa^{(k)}(\Xi))(\mathbf{x}_i^{(k)}) - \hat{u}(\mathbf{x}_i^{(k)}; \kappa^{(k)}) \right|^2. \quad (8)$$

The Physics-Informed Deep Operator Network (PI-DeepONet or PI-DON; referred to as PI-DON in this paper) [24] integrates the idea of physics-informed neural networks (PINN) [19] with the DeepONet framework. The PI-DON introduces the additional PDE residual loss function and boundary condition loss function. Consequently, the loss function for PI-DON is defined as

$$\mathcal{L}(\theta) = w_{\text{data}} \mathcal{L}_{\text{data}}(\theta) + w_{\text{PDE}} \mathcal{L}_{\text{PDE}}(\theta) + w_{\text{bc}} \mathcal{L}_{\text{bc}}(\theta), \quad (9)$$

where $\mathcal{L}_{\text{PDE}}(\theta)$ denotes the PDE residual loss, $\mathcal{L}_{\text{bc}}(\theta)$ the boundary condition loss, and w_{data} , w_{PDE} , and w_{bc} are the corresponding weights for each term.

2.3 Multi-objective Optimization

To obtain the optimal PI-DON, i.e., minimizing the multi-objective loss function in (9), one needs to consider to solving a multi-objective optimization problem. In fact, multi-objective optimization problems frequently arise in various scientific and engineering fields [36, 37, 38, 39, 40, 41, 42, 43], many of which involve high-dimensional spaces. In this paper, we propose a refined version of the nondominated sorting genetic algorithm (refined NSGA-III) that builds upon the classical NSGA-III framework originally introduced by [30]. The refined NSGA-III retains the population-based evolutionary structure designed for multi-objective optimization while incorporating additional mechanisms to improve sampling diversity in the operator learning settings.

2.3.1 Nondominated Sorting Genetic Algorithm (NSGA-III)

To illustrate the NSGA-III algorithm, we begin with the general problem setting: Given $m \in \mathbf{N}$, the m -objective function is defined as $f(x) = (f_1(x), \dots, f_m(x))$ where $x \in \Omega$, and $f_i: \Omega \rightarrow \mathbf{R}$ for a given search space Ω . Different from single-objective optimization, there is usually no solution that minimizes all m objective functions simultaneously. To make it easier for comparison, we define the solution x *dominates* the solution y , denoted as $x \preceq y$ if and only if $f_j(x) \leq f_j(y)$ for all $1 \leq j \leq m$. A solution is referred as *Pareto-optimal* if it is not strictly dominated by any other solution. Here, the set of objective values of Pareto-optimal solutions is denoted as *Pareto front*. The NSGA-III algorithm, originally proposed by Deb and Jain [44], belongs to the evolutionary optimization framework and incorporates external mechanisms to support diversity maintenance, which can also help reduce the computational burden. Instead of exhaustively exploring the entire search space for Pareto-optimal solutions, the algorithm initiates multiple predefined, targeted searches. More specifically, NSGA-III initializes with a random population of size N_{mo} . In each subsequent iteration, one can generate a size N_{mo} offspring population with mutation and/or crossover operators. With a fixed population size, NSGA-III selects N_{mo} individuals for the next iteration from the combined pool of $2N_{mo}$ candidates. Since non-dominated solutions are used, a ranking scheme is employed in which dominance serves as the primary criterion for survival. Individuals that are not strictly dominated by any other member of the population are assigned rank 1. Subsequent ranks are determined recursively: each unranked individual that is strictly dominated only by those with ranks $1, \dots, k-1$ is assigned rank k . Intuitively, the lower an individual's rank, the more interesting it is. Denote F_i be the set of individuals with rank i , and let i^* be the smallest integer such that

$$\sum_{i=1}^{i^*} |F_i| \geq N_{mo}. \quad (10)$$

All individuals with rank at most $i^* - 1$ retain to the next generation. In addition, $0 < k \leq N_{mo}$ individuals of rank i^* must be selected so that the new population remains N_{mo} , allowing the next iteration to proceed.

Algorithm 1 Nondominated Sorting Genetic Algorithm (NSGA-III)

Require: Population size N , number of generations G , reference directions R

Ensure: Optimized Pi-FDON models on Pareto front

- 1: Initialize population P_0 with N candidate Pi-FDON models
 - 2: Evaluate objectives $\mathbf{F}(x)$ for all $x \in P_0$
 - 3: **for** $t = 0$ to $G - 1$ **do**
 - 4: Generate offspring Q_t using crossover and mutation operation
 - 5: Evaluate objectives $\mathbf{F}(x)$ for all $x \in Q_t$
 - 6: $R_t \leftarrow P_t \cup Q_t$ ▷ Combine parent and offspring
 - 7: Perform non-dominated sorting on R_t to obtain fronts F_1, F_2, \dots
 - 8: Initialize $P_{t+1} \leftarrow \emptyset, i \leftarrow 1$
 - 9: **while** $|P_{t+1}| + |F_i| \leq N$ **do**
 - 10: $P_{t+1} \leftarrow P_{t+1} \cup F_i$
 - 11: $i \leftarrow i + 1$
 - 12: **end while**
 - 13: Normalize objectives of F_i
 - 14: Associate each solution in F_i with closest reference direction in R
 - 15: Compute niche count for each reference direction
 - 16: **while** $|P_{t+1}| < N$ **do**
 - 17: Select reference direction with minimum niche count
 - 18: Choose one associated solution (random if tie) and add to P_{t+1}
 - 19: **end while**
 - 20: **end for**
 - 21: **return** Final Pareto front P_G
-

2.3.2 Refined Nondominated Sorting Genetic Algorithm (RNSGA-III)

The vanilla NSGA-III algorithm (1), when applied to operator learning for PDEs problems, tends to minimize the multi-objective loss functions (9). In principle, NSGA-III does not inherently “contract” samples to a local region of the front. In practice, however, it is common to observe a non-dominated set on a local sub-arc (or sub-face) of the attainable front. This phenomenon is not a theoretical property of the algorithm but typically arises from the following possible perspectives: (i) a mismatch between the fixed reference directions and the shape/location of the optimal Pareto

front such that many directions do not intersect the feasible front [45, 46], (ii) poor objective normalization or strong scale differences that is usual in operator learning setting, introduces a bias into the perpendicular-distance association step [47], (iii) high correlation among objectives in operator learning [48], e.g., \mathcal{L}_{PDE} and \mathcal{L}_{BC} can be closely related, that can reduce the effective dimensionality of the front, and (iv) feasibility/constraint handling overpowering diversity pressure so that selection repeatedly favors a small subset of niches [49, 50]. The choice of stochastic mini-batching of residual and boundary losses can further amplify these effects, because the noise it introduces may affect dominance checks, i.e., comparisons used to determine whether one solution is better than another, and association steps, i.e., the process of assigning solutions to reference directions or niches. Figure 3 illustrates such cases, where the vanilla NSGA-III produces sampling points (green points) concentrated within a local sub-face of the attainable Pareto front.

To overcome this limitation, we propose the refined NSGA-III, which integrates the refined Pareto sampling (RPS) strategy into the original NSGA-III framework. At each iteration, the RPS first identifies solutions with sufficiently distinct objective values and then selects a representative subset based on pairwise distances between their outputs. The details of the RPS strategy is described in Algorithm 2 and the red sampling points in Figure 3 illustrate the RPS sampling in contrast to the vanilla NSGA-III sampling (green points).

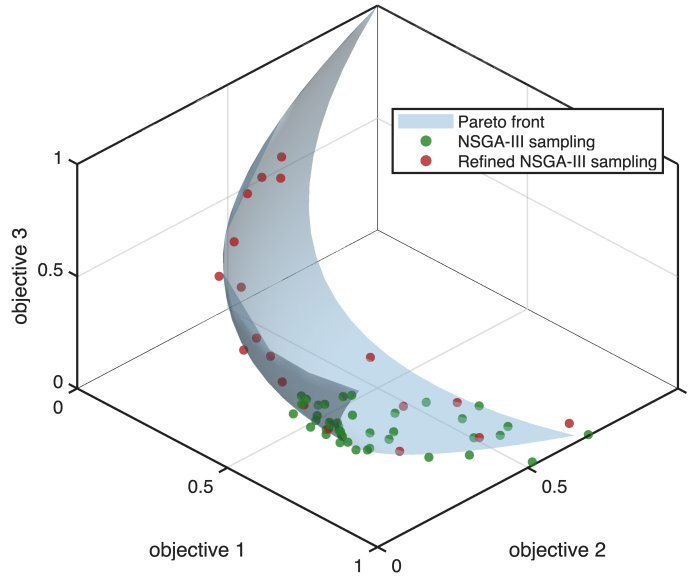


Figure 3: Illustration of NSGA-III and refined NSGA-III sampling near the Pareto front.

Algorithm 2 Refined Pareto Sampling (RPS)**Require:** Pareto front $\mathcal{P} \in \mathbb{R}^{M \times K}$, number of models to select N_{sel} , optional distance threshold ϵ **Ensure:** Selected set of models \mathcal{S}

```

1: Initialize  $\mathcal{S} \leftarrow \emptyset$ 
2:                                     ▷ Step 1: Select extreme models
3: for  $k = 1$  to  $K$  do
4:    $i^* \leftarrow \arg \min_i \mathcal{P}[i, k]$                                      ▷ Model with lowest objective  $k$ 
5:    $\mathcal{S} \leftarrow \mathcal{S} \cup \{\mathcal{P}[i^*]\}$ 
6: end for
7:  $\mathcal{R} \leftarrow \mathcal{P} \setminus \mathcal{S}$                                      ▷ Remaining models
8:                                     ▷ Step 2: Select diverse models
9: while  $|\mathcal{S}| < N_{\text{sel}}$  and  $\mathcal{R} \neq \emptyset$  do
10:  for each model  $r \in \mathcal{R}$  do
11:     $d_r \leftarrow \min_{s \in \mathcal{S}} \text{distance}(\mathcal{P}[r, :], s)$ 
12:  end for
13:   $r^* \leftarrow \arg \max_r d_r$                                      ▷ Farthest model from selected set
14:  if  $d_{r^*} > \epsilon$  or  $\epsilon$  not defined then
15:     $\mathcal{S} \leftarrow \mathcal{S} \cup \{\mathcal{P}[r^*]\}$ 
16:  end if
17:   $\mathcal{R} \leftarrow \mathcal{R} \setminus \{\mathcal{P}[r^*]\}$ 
18: end while
19: return  $\mathcal{S}$ 

```

2.4 Replica Exchange Stochastic Gradient Langevin dynamics

Replica exchange stochastic gradient Langevin dynamics (reSGLD) [51] extends the classical stochastic gradient Langevin dynamics (SGLD) [52] by incorporating the replica exchange mechanism from statistical physics. While SGLD is a scalable Markov Chain Monte Carlo (MCMC) method that interpolates between stochastic optimization and posterior sampling as the step size decreases, its efficiency is often limited by the pathological curvature of the underlying energy landscape that may lead to local trapping. To reconcile this issue, reSGLD employs multiple diffusion processes at different temperatures and operates occasional swaps which can enable high-temperature replicas to traverse energy barriers and facilitate exploration across distinct local modes. This mechanism which combines the scalability of SGLD with the efficiency of replica exchange leads to accelerated convergence, which has been both theoretically established [53, 54] and empirically validated [51].

To illustrate the reSGLD algorithm, we first recall the negative log-posterior (energy function) given by

$$L(\boldsymbol{\beta}) = -\log p(\boldsymbol{\beta}) - \sum_{i=1}^N \log P(\mathbf{d}_i | \boldsymbol{\beta}), \quad (11)$$

where $p(\boldsymbol{\beta})$ is the prior and the second term corresponds to the complete-data log-likelihood. For large datasets, direct evaluation is expensive and sometimes prohibitive. A common remedy is to approximate it using a mini-batch $\mathcal{B} = \{\mathbf{d}_{s_i}\}_{i=1}^n$, which yields an unbiased stochastic energy estimator:

$$\tilde{L}(\boldsymbol{\beta}) = -\log p(\boldsymbol{\beta}) - \frac{N}{n} \sum_{i=1}^n \log P(\mathbf{d}_{s_i} | \boldsymbol{\beta}). \quad (12)$$

The stochastic gradient Langevin dynamics (SGLD) iterates as

$$\boldsymbol{\beta}^{(k+1)} = \boldsymbol{\beta}^{(k)} - \eta^{(k)} \nabla \tilde{L}(\boldsymbol{\beta}^{(k)}) + \sqrt{2\eta^{(k)}\tau_1} \boldsymbol{\xi}^{(k)}, \quad (13)$$

where $\eta^{(k)}$ is the learning rate and $\boldsymbol{\xi}^{(k)}$ is a standard Gaussian noise. As $\eta^{(k)} \rightarrow 0$, SGLD converges to the invariant distribution $\pi(\boldsymbol{\beta}) \propto \exp(-L(\boldsymbol{\beta})/\tau_1)$. A naive extension of replica exchange Langevin dynamics (reLD) to the stochastic gradient setting leads to the following two-chain system:

$$\begin{aligned} \boldsymbol{\beta}^{(1,k+1)} &= \boldsymbol{\beta}^{(1,k)} - \eta^{(k)} \nabla \tilde{L}(\boldsymbol{\beta}^{(1,k)}) + \sqrt{2\eta^{(k)}\tau_1} \boldsymbol{\xi}^{(1,k)}, \\ \boldsymbol{\beta}^{(2,k+1)} &= \boldsymbol{\beta}^{(2,k)} - \eta^{(k)} \nabla \tilde{L}(\boldsymbol{\beta}^{(2,k)}) + \sqrt{2\eta^{(k)}\tau_2} \boldsymbol{\xi}^{(2,k)}, \end{aligned} \quad (14)$$

where $\tau_1 < \tau_2$ are different temperatures. Replica exchange is then attempted by swapping the two chains with a naive stochastic swapping rate

$$\mathbb{S}(\boldsymbol{\beta}^{(1,k+1)}, \boldsymbol{\beta}^{(2,k+1)}) = \exp\left[\left(\frac{1}{\tau_1} - \frac{1}{\tau_2}\right) (\tilde{L}(\boldsymbol{\beta}^{(1,k+1)}) - \tilde{L}(\boldsymbol{\beta}^{(2,k+1)}))\right]. \quad (15)$$

However, the stochastic estimates $\tilde{L}(\cdot)$ enter (15) through a nonlinear exponential, which introduces significant bias in the swap acceptance probability. This bias breaks detailed balance and results in poor approximation of the target distribution. To address this, a correction is introduced by modeling the stochastic energy difference as a Gaussian perturbation,

$$\tilde{L}(\boldsymbol{\beta}^{(1)}) - \tilde{L}(\boldsymbol{\beta}^{(2)}) = L(\boldsymbol{\beta}^{(1)}) - L(\boldsymbol{\beta}^{(2)}) + \sqrt{2}\sigma W_1, \quad (16)$$

where $W_1 \sim \mathcal{N}(0, 1)$. This yields the corrected swap acceptance rate

$$\tilde{\mathbb{S}}_1 = \exp\left[\left(\frac{1}{\tau_1} - \frac{1}{\tau_2}\right) \left(\tilde{L}(\boldsymbol{\beta}^{(1)}) - \tilde{L}(\boldsymbol{\beta}^{(2)}) - \left(\frac{1}{\tau_1} - \frac{1}{\tau_2}\right)\sigma^2\right)\right], \quad (17)$$

which is now an unbiased estimator of the exact acceptance probability. The correction term $\left(\frac{1}{\tau_1} - \frac{1}{\tau_2}\right)\sigma^2$ compensates for the variance of the mini-batch noise and restores the validity of the replica exchange procedure.

2.5 Uncertainty Quantification

Uncertainty quantification (UQ) is critical to ensure the reliability of machine learning models in scientific applications. The reSGLD mechanism inherent in the Morephy-Net framework provides a natural and efficient way to perform Bayesian UQ. By sampling the posterior distribution of the model parameters θ using reSGLD, we obtain an ensemble of model predictions that can be used to quantify uncertainty. Specifically, the predictive mean and variance are given by $\bar{u}(x, t) = \frac{1}{N_s} \sum_{i=1}^{N_s} G_{\theta_i}(\kappa)(x, t)$ and variance $\sigma^2(x) = \frac{1}{N_s-1} \sum_{i=1}^{N_s} (G_{\theta_i}(\kappa)(x, t) - \bar{u}(x, t))^2$, where N_s denotes the sample size and $G_{\theta_i}(\kappa)(x, t)$ is the prediction from the i th sampled model.

3 Numerical Results

In this section, we will show the numerical test results for the proposed Morephy-Net in both forward and inverse problem setting. Specifically, we consider two different test problems: the one-dimensional viscous Burgers' equation and the one-dimensional time-fractional mixed diffusion-wave equations (TFMDWEs). The inverse problem settings are formulated to identify the viscosity parameter in the Burgers' equation and the fractional derivative order in the TFMDWEs. To avoid ambiguity, we provide a summary in Table 1 that lists all the models used for comparison with Morephy-Net in the numerical tests, along with their full names.

Table 1: Summary of models used in numerical tests. Acronyms: DeepONet = Deep Operator Network; PI-DON = Physics-informed Deep Operator Network; PI-FDON = Physics-informed Fourier Deep Operator Network; Morephy-Net = Multi-Objective Replica Exchange Physics-informed Deep Operator Network.

Acronym	Physics-informed	Uncertainty Quantification	Fourier Feature
DeepONet	–	–	–
PI-DON	Yes	–	–
PI-FDON	Yes	–	Yes
Morephy-Net	Yes	Yes	Yes

3.1 Burgers' Equation

The one-dimensional viscous Burgers' equation is a nonlinear partial differential equation frequently used as a benchmark [55, 56, 19, 57]. The equation with Dirichlet boundary conditions, is defined on the spatial domain $\Omega = [-1, 1]$ and temporal domain $[0, T]$ given by the following:

$$\frac{\partial u}{\partial t} - \nu \frac{\partial^2 u}{\partial x^2} + u \frac{\partial u}{\partial x} = 0, \quad x \in \Omega, t \in [0, T], \quad (18)$$

$$u(x, t) = 0, \quad \forall x \in \partial\Omega, \quad (19)$$

$$u(x, 0) = -\sin(\pi x). \quad (20)$$

Here, $u(x, t)$ represents the solution over space and time, and ν is the viscosity chosen to be $0.01/\pi$.

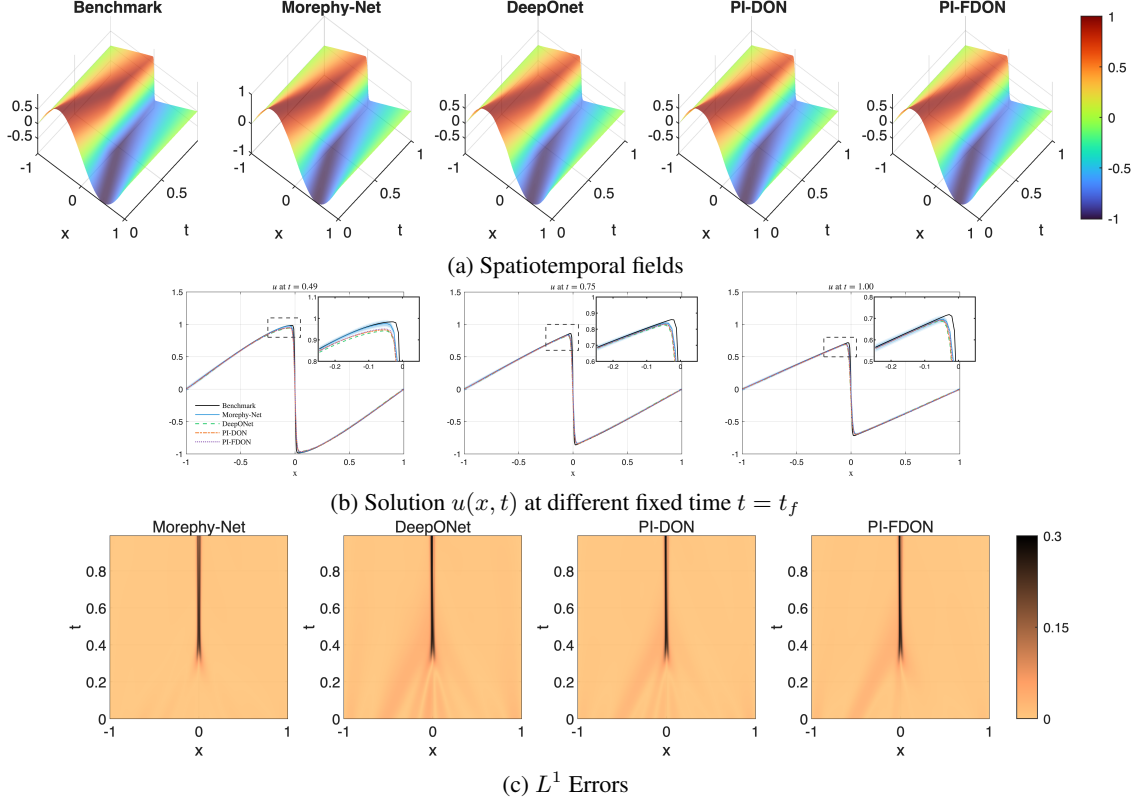


Figure 4: Comparisons of different models (DeepONet, Pi-DON, Pi-FDON, and Morephy-Net) and benchmark solutions for the forward Burgers problem. Panel (a). Spatiotemporal fields of the solutions. Panel (b). Solutions at different fixed time instances $t = t_f$. Panel (c). L^1 errors.

3.1.1 Hyperparameters

To ensure a rigorous and unbiased comparison between DeepONet, Pi-DON, and Pi-FDON, we standardized the core architecture and training protocol across all models. For each network, both the branch and trunk sub-networks were constructed as Multi-Layer Perceptrons (MLPs) featuring a depth of 8 hidden layers and a width of 50 neurons per layer. The training regimen was also held constant for all experiments. We employed the Adam optimizer with a learning rate of $5e-4$. To mitigate overfitting and improve training efficiency, an early stopping criterion was implemented, which terminated the training process if the validation loss did not demonstrate significant improvement over a predefined number of epochs.

3.1.2 Forward Problem

We solve the forward problem for the 1D viscous Burgers' equation to evaluate the performance of four models: DeepONet, Pi-DON, and Pi-FDON. The goal is to predict the solution $u(x, t)$ for the entire spatio-temporal domain $(x, t) \in [-1, 1] \times [0, 1]$, given the initial and boundary conditions. The visualization results are presented in Figure 4. As shown in first row 4a, all four models successfully learn the overall dynamics of the Burgers' equation. The 3D spatiotemporal plots demonstrate that each model captures the smooth initial state and the subsequent formation of a steep shock front as time progresses. A more detailed analysis is presented in second row 4b presents solution snapshots at time $t = 0.49$, $t = 0.75$ and $t = 1.00$, revealing significant performance differences in resolving the shock front discontinuity. The prediction from Morephy-Net, shown as a blue shaded region representing the 95% confidence interval, almost perfectly overlaps the benchmark solution. It captures the sharp shock wave with no visible overshooting or spurious oscillations, yielding a stable and physically plausible result. In the contrast, the other three models struggle to resolve the sharp gradient. As highlighted in the insets, these models exhibit non-physical oscillations near the shock, an issue that becomes more pronounced as the shock steepens over time. The L_1 error distributions are plotted in third row 4c. The errors for DeepONet, Pi-DON, and Pi-FDON are heavily concentrated along the trajectory of the shock wave. The error map for Morephy-Net is visibly lighter, indicating a lower error magnitude across the domain and reinforcing its superior performance in shock capturing. The quantitative performance of the models is

summarized in Table 2 to clearly illustrate the model difference. As from our observation, the proposed Pi-FDON shows higher accuracy than DON and Pi-DON model. Crucially, the Morephy-Net model demonstrates the best performance overall. It better satisfies the residual constraint and boundary constraint and also achieves the lowest relative L_2 error.

Table 2: Losses and Errors of different models in the 1D Burgers Equation forward problem.

Model	Residual Loss	IBC Loss	L_2 relative error
DeepONet	N/A	0.0008	0.0550
Pi-DON	0.0007	0.0003	0.0510
Pi-FDON	0.0004	0.0003	0.0446
Morephy-Net	0.0002	0.0001	0.0436

3.1.3 Inverse Problem

We now focus on the inverse problem for Burgers’ equation, a more challenging task where the viscosity parameter, v , is treated as an unknown variable. Our objectives are to infer the correct value of the viscosity parameter v and accurately reconstruct the full continuous solution field $u(x, t)$ over the entire spatial-temporal domain. This type of parameter inference poses a significant challenge for deep learning models. The complex and non-convex loss landscapes associated with inverse problems mean that the optimization process can easily become trapped in poor local minima, leading to inaccurate parameter estimates and solution reconstructions. We use the observational data serve as anchors during the training process, ensuring that the network remains consistent with the underlying physical dynamics. In the inverse problem, the total loss function is composed of three components: the PDE residual loss, the boundary and initial condition loss, and the data loss.

In Figure 5, the first row 5a, shows the reconstruction result in the spatial-temporal solution field. The second row 5b shows the snapshot of the result at three distinct timesteps. As shown in this figure, the prediction of DeepONet shows the most severe oscillations, above the benchmark at $t = 0.49$ and $t = 1.00$ but below the benchmark at $t = 0.75$. Pi-DON and Pi-FDON also fail to produce a clean, stable prediction. However, Morphy-Net demonstrates best performance in this scenario. The blue shaded region shows the 95% confidence interval and it almost perfectly overlaps the black benchmark line. It has a great improvement when compare with the other three models. The third row 5c displays a comparison of error heatmaps for four models. Each plot visualizes the absolute error between the model’s prediction and the true solution over a 2D domain of space x and time t . As we can observe from the figure that the Morphy-Net performs the best accuracy. the lighter bright line along the center indicates a lower error that is concentrated where the shock wave occurs.

Table 3: Model performance for the Burgers’ inverse problem. For reference, the truth value of $v = 0.01/\pi \approx 0.00318$

Model	Residual	IBC loss	Data loss	Predicted v	L_2 relative error
DeepONet	N/A	0.0007	0.0009	0.0161	0.1174
Pi-DON	0.0010	0.0043	0.0015	0.0098	0.0700
Pi-FDON	0.0008	0.0026	0.0008	0.0073	0.0560
Morephy-Net	0.0003	0.0005	0.0001	0.0062	0.0358

Table 3 shows the numerical difference on the performance of each model. Morephy-Net emerges as the most effective architecture. It excels in both aspects of the task: its predicted viscosity v (0.0062) is the closest to the ground truth, and its corresponding solution reconstruction is the most accurate. This is evidenced by its L_2 relative error of 0.0358, significantly smaller than Pi-FDON which is 0.0560.

3.1.4 Inverse Problem With Noisy Data

We now investigate a more challenging version of the inverse problem to assess model robustness. The sparse training data are corrupted by adding noise drawn from a Gaussian distribution with a zero mean. We introduce a substantial noise level by setting the noise’s standard deviation to 50% of the standard deviation of the true data, evaluating the models’ capacity to learn the governing physics from corrupted observations.

Figure 6 shows the reconstructed solution and error in the spatial-temporal domain. In the second row 6b, the Morphy-Net model shows good performance and reliability. The prediction of Morphy-Net is visualized as a blue shaded area, representing the 95% confidence interval in second row 6b. As clearly shown in the zoomed in figure, this confidence

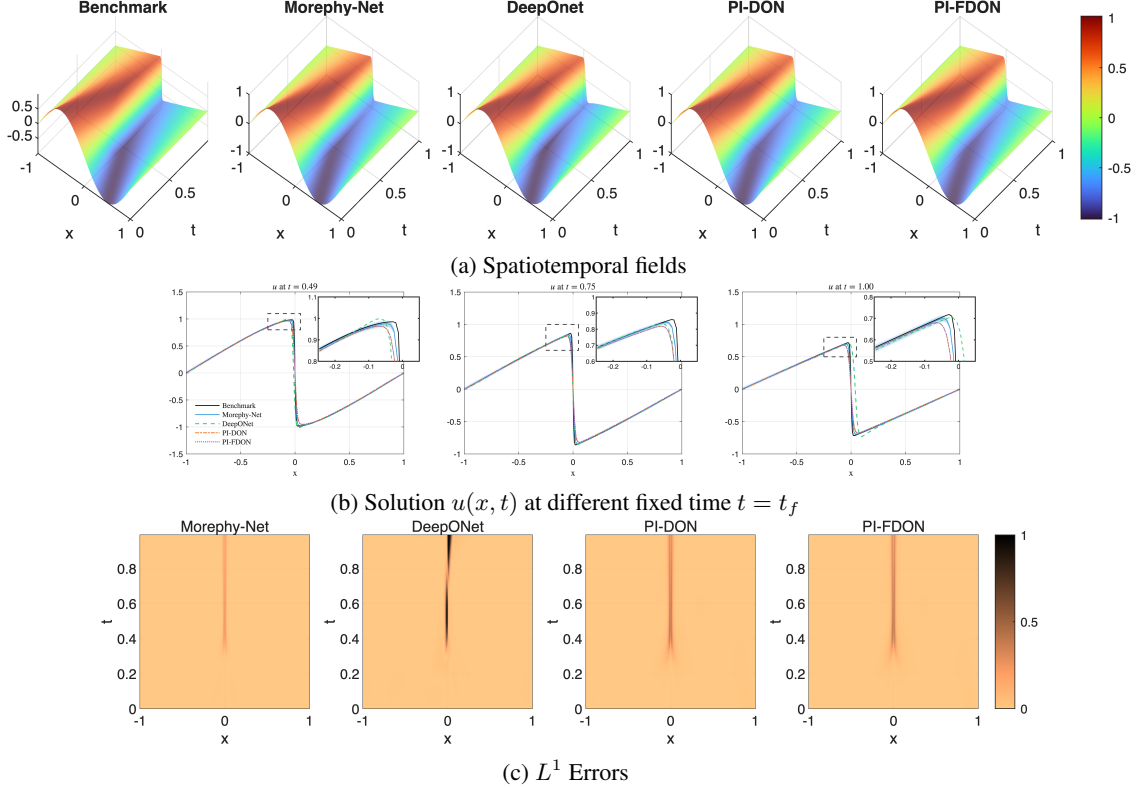


Figure 5: Comparisons of different models (DeepONet, Pi-DON, Pi-FDON, and Morephy-Net) and benchmark solutions for the inverse Burgers problem. Panel (a). Spatiotemporal fields of the solutions. Panel (b). Solutions at different fixed time instances $t = t_f$. Panel (c). L^1 errors.

interval covers black benchmark line from $x = -1$ to 0 . In the contrast, the other three models fail to accurately capture the shock. Their point predictions exhibit significant deviations and spurious oscillations near the discontinuity. The spatial-temporal L_1 error distribution for four models are shown in the third row 6c. The Morphy-Net error map is lighter than others, indicates a substantially lower prediction error across the entire space-time domain. Table 4 summarizes the results for the challenging inverse problem with noisy data, where Morephy-Net shows the most robust performance. It not only achieves the best fit to the physical and data constraints but also yields the most accurate parameter prediction (0.0063). Consequently, it achieves a significantly lower L_2 relative error of 0.0744 compare with Pi-FDON of 0.1249.

Table 4: Model performance for the Burgers’ inverse problem with noisy data.

Model	Residual Loss	IBC loss	Data loss	Predicted v	L_2 relative error
DeepONet	N/A	0.0068	0.5762	0.0086	0.1421
Pi-DON	0.0084	0.0042	0.3461	0.0078	0.1260
Pi-FDON	0.0074	0.0026	0.4653	0.0073	0.1249
Morephy-Net	0.0043	0.0021	0.2713	0.0063	0.0744

3.2 Time-fractional Mixed Diffusion-Wave Equations (TFMDWEs)

In this section, we consider the *time-fractional mixed diffusion-wave equations* (TFMDWEs), which generalize classical diffusion and wave equations by incorporating fractional-order time derivatives [58, 59, 60]. The TFMDWEs with

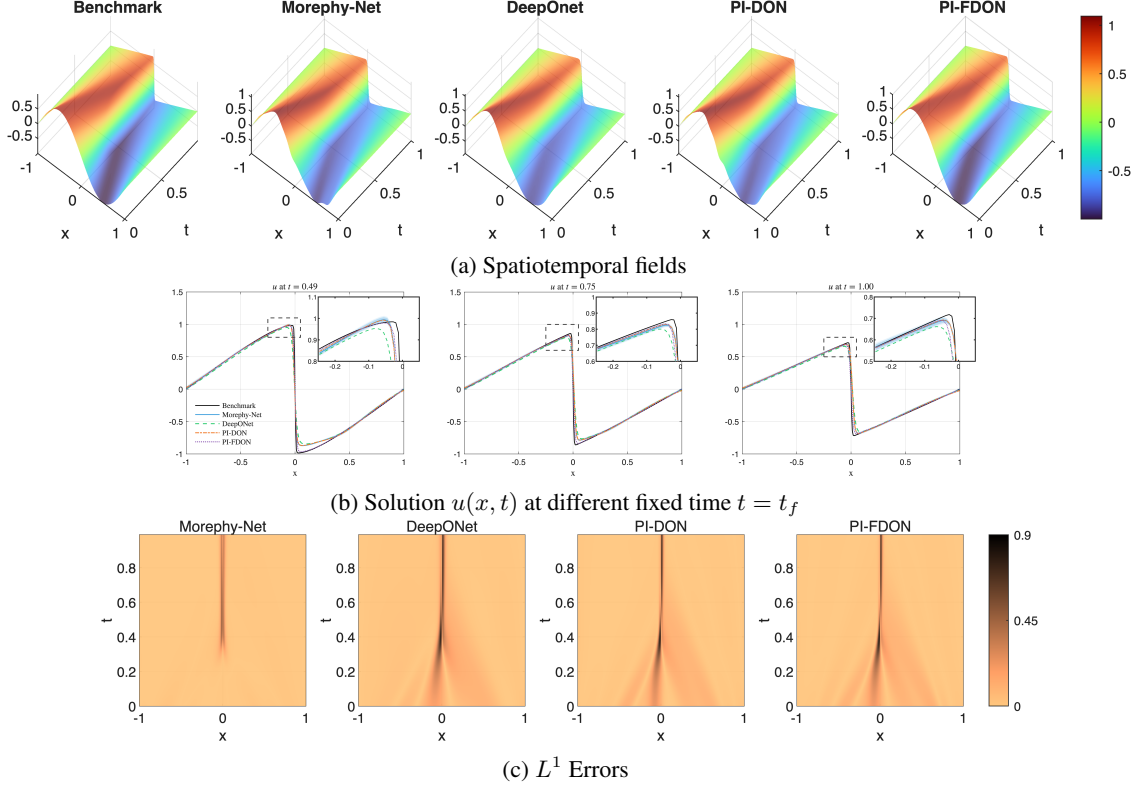


Figure 6: Comparisons of different models (DeepONet, Pi-DON, Pi-FDON, and Morephy-Net) and benchmark solutions for the inverse Burgers problem with noisy observation data. Panel (a). Spatiotemporal fields of the solutions. Panel (b). Solutions at different fixed time instances $t = t_f$. Panel (c). L^1 errors.

Dirichlet boundary conditions are defined as follows:

$$D_t^\alpha u(x, t) = \frac{\partial^2 u}{\partial x^2} + f(x, t), \quad t \in [0, 1], \quad x \in [0, \pi], \quad (21)$$

$$u(x, t) = 0, \quad \forall x \in \partial\Omega, \quad (22)$$

$$u(x, 0) = 0, \quad x \in \Omega, \quad (23)$$

where the fractional order α yields: $\alpha \in [0, 1]$, $\forall t \in [0, 1]$, and the forcing term $f(x, t)$ is explicitly defined as:

$$f(x, t) = \frac{\Gamma(4)}{\Gamma(4 - \alpha)} t^{3-\alpha} \sin(x) + t^3 \sin(x), \quad (24)$$

with $\Gamma(\cdot)$ denoting the Gamma function. This equation introduces fractional-order temporal dynamics, combining features of both diffusion and wave phenomena. The fractional order α controls the transition between diffusive and wave-like behaviors, making TFMDWEs particularly useful in modeling complex systems exhibiting anomalous transport and non-local temporal interactions.

3.2.1 Hyperparameters

To ensure a fair comparison between DeepONet, Pi-DON, and Pi-FDON, we standardized the core architecture and training protocol across all models. For each network, both the branch and trunk sub-networks were constructed as Multi-Layer Perceptrons (MLPs) featuring a depth of 3 hidden layers and a width of 100 neurons per layer. The training regimen was also held constant for all experiments. We employed the Adam optimizer with a learning rate of $5e-4$. The early stopping criterion was implemented to mitigate overfitting and improve training efficiency.

3.2.2 Forward Problem

This section details the performance evaluation of the four models—Morephy-Net, DeepONet, Pi-DON, and Pi-FDON—on the forward problem. A comprehensive comparison against the benchmark solution is presented in Figure 7,

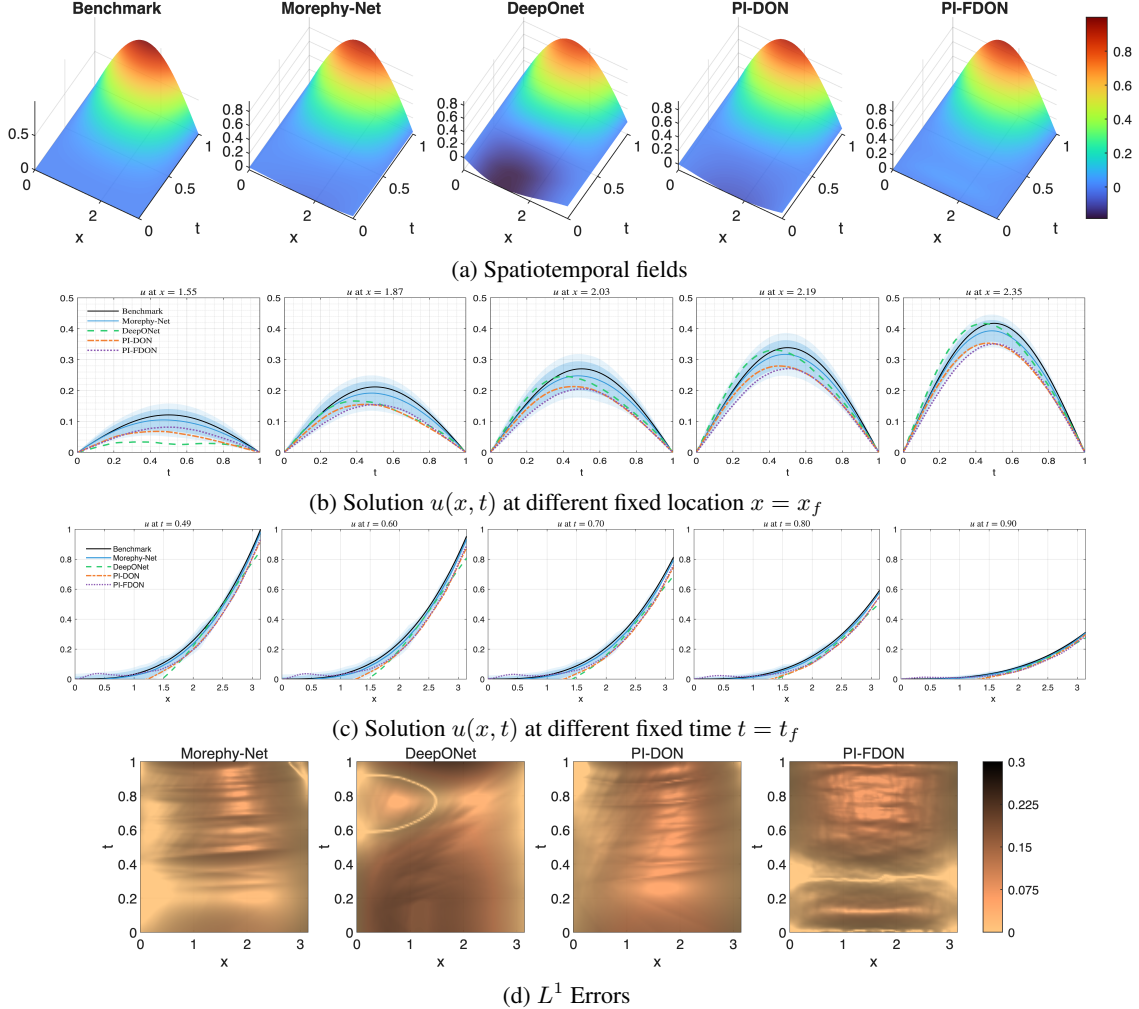


Figure 7: Visual comparison of models for the forward TFMDWEs. The ground truth solution is compared against predictions from DON, Pi-DON, Pi-FDON and Morphy-Net

which includes spatiotemporal field reconstructions, solution cross-sections, and quantitative error distributions. The collective results demonstrate the superior accuracy and reliability of the Morphy-Net architecture. Figure 7a provides a comparison of the full spatiotemporal solution fields. The predictions generated by Morphy-Net, PI-DON, and PI-FDON are visually indistinguishable from the benchmark, indicating that they have successfully learned the underlying dynamics of the system. In contrast, the DeepOnet model exhibits a noticeable deviation, with a significant error concentrated near the initial condition at $t = 0$, suggesting a failure to correctly capture the initial state of the system. Figures 7b and Figure 7c display solution cross-sections at various fixed spatial locations (x_f) and temporal snapshots (t_f) respectively. The 95% confidence interval of the Morphy-Net prediction, represented by the blue shaded region, consistently envelops the ground truth benchmark line across all subplots. This demonstrates that the true solution lies within the model’s predicted uncertainty bounds. On the contrary, we can observe the predictions result of other models are lower than the benchmark at fixed location shown in 7b and predictions are deviate from the benchmark shown in 7c. Figure 7d shows the L_1 error heatmaps. The error map for Morphy-Net is visibly lighter in color across the entire spatiotemporal domain, indicating a significantly lower overall prediction error compared to the other models.

Table 5 demonstrate a consistent trend of improvement within the operator-learning architectures. The Morphy-Net stands out as the most accurate architecture. It achieves the lowest L_2 relative error of 0.0935, a substantial improvement over the best-performing operator-learning model. It also records the lowest Initial and Boundary Condition (IBC) loss, indicating its superior ability to satisfy the problem’s constraints.

Table 5: Model performance for the forward TFMDWEs.

Model	Residual loss	IBC loss	L_2 relative error
DON	0.0903	0.0173	0.3080
Pi-DON	0.0703	0.0153	0.1620
Pi-FDON	0.0539	0.0148	0.1319
Morephy-Net	0.0672	0.0112	0.0935

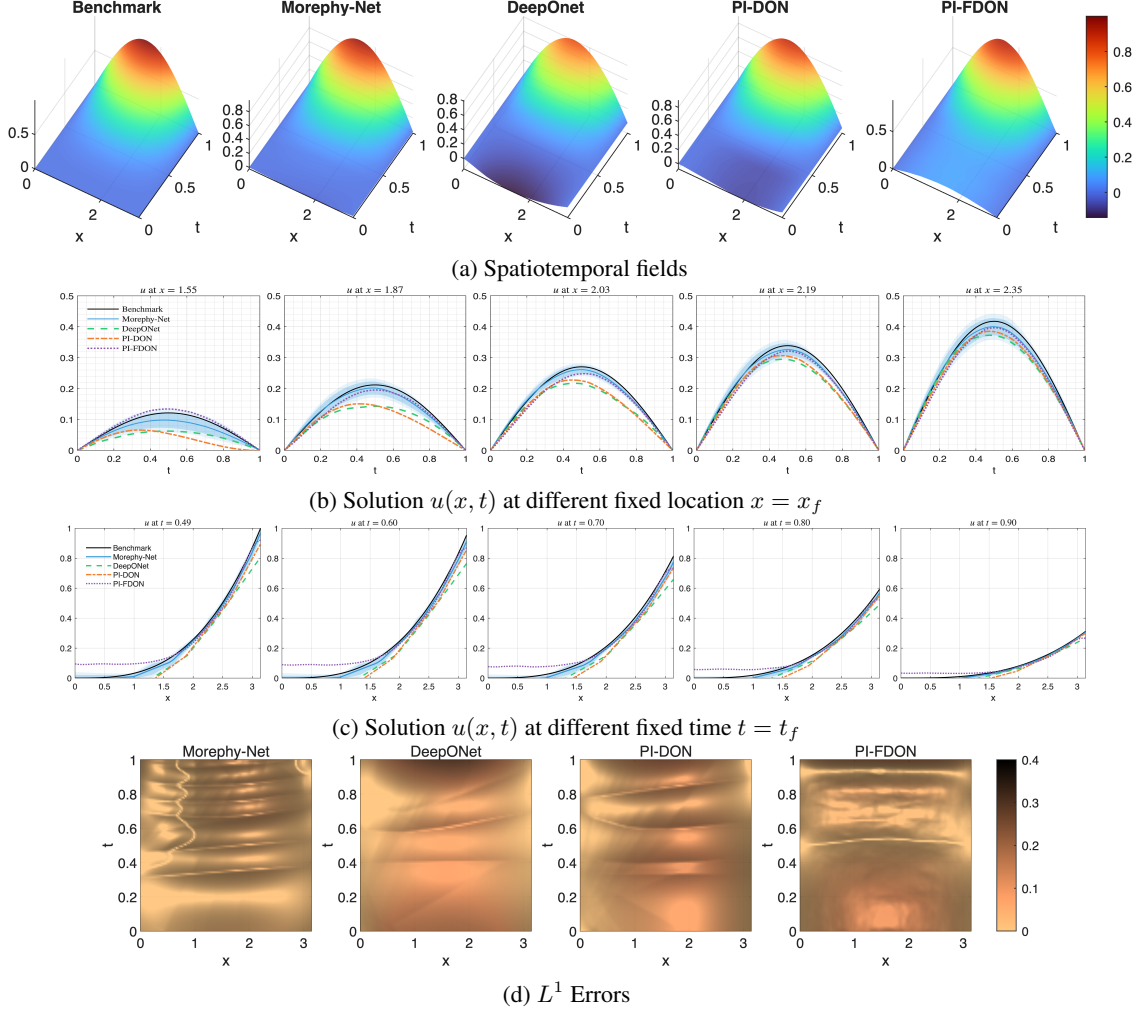


Figure 8: Visual comparison of models for the inverse TFMDWEs. The ground truth is compared against predictions from DON, Pi-DON, Pi-FDON and Morphy-Net

3.2.3 Inverse Problem

We assume the fractional order is known in Time-fractional Mixed Diffusion-Wave Equations and build model to learn the fractional and reconstruct the solution. Figure 8 shows the visualization result. In the first row, we show the reconstructed result from different models and compare with the benchmark. From our observation, the Morphy-Net solution clearly match with the benchmark whereas the reconstructed solutions from other three models have mismatch at $x = 0$ and $t = 0$. The second and third row shows projection os solution in 2D at different location and time. These figures show that the Morphy-Net can cover the benchmark in its 95% confidence interval (dark blue shadow). The fourth row shows the L_1 heatmap of these four models. The Morphy-Net shows lighter color than other models.

Table 6: Model performance for the inverse TFMDWEs

Model	Residual Loss	IBC Loss	Data Loss	Predicted α	L_2 relative error
DON	0.0641	0.0275	0.0503	0.6930	0.2298
Pi-DON	0.0541	0.0148	0.0499	0.6640	0.1813
Pi-FDON	0.0509	0.0151	0.0458	0.5954	0.1359
Morephy-Net	0.0236	0.0148	0.0384	0.5740	0.1134

4 Conclusion and Future Work

In this paper, we introduced Morephy-Net, a new framework for physics-informed operator learning. By integrating an evolutionary multi-objective optimization algorithm (refined NSGA-III) with replica exchange stochastic gradient Langevin dynamics (reSGLD), Morephy-Net effectively balances data loss and physics loss, enhances global exploration of the parameter space, and provides robust uncertainty quantification. Numerical tests on the Burgers’ equation and the time-fractional mixed diffusion-wave equation showed that the Morephy-Net is more accurate than the standard operator learning methods, such as DeepONet, PI-DON, et al, in forward, inverse, and noisy data scenarios. Moreover, the Morephy-Net provides effective uncertainty quantification where the standard operator learning methods can rarely provide.

There are several promising future directions that are worth further investigation. First, extending the multi-objective replica exchange physics informed setting to evolutionary Kolmogorov–Arnold networks[61, 62] provides a natural integration of physics-informed evolutionary operator learning with Kolmogorov–Arnold networks, which can potentially improve expressiveness and interpretability. Second, the Morephy-Net, with its inherent uncertainty quantification (UQ) capability, can be further explored in data assimilation (DA) settings, where accurate state estimation with model uncertainty is essential for high-dimensional dynamical systems [63, 64, 65, 66, 67, 68]. Since DA usually requires running a large number of repeated forecasts in an ensemble or iterative framework, the operator-learning framework of Morephy-Net provides a computationally efficient surrogate for the underlying dynamics. This efficiency, combined with its UQ features, makes it particularly well-suited for DA with observational data in real time. Third, applying Morephy-Net to turbulent flows governed by the Navier–Stokes equations (NSE) offers an exciting opportunity to test its robustness and scalability in highly nonlinear and multiscale systems [69, 70, 71].

Acknowledgment

We would like to thank the support of National Science Foundation (DMS-2053746, DMS-2134209, ECCS-2328241, CBET-2347401 and OAC-2311848), and U.S. Department of Energy (DOE) Office of Science Advanced Scientific Computing Research program DE-SC0023161, and DOE–Fusion Energy Science, under grant number: DE-SC0024583.

Github codes

The source code for Morphy-Net is available at: <https://github.com/jeremy1u916/MORPHY-Net>

References

- [1] L. C. Evans, *Partial differential equations*. American mathematical society, 2022, vol. 19.
- [2] W. A. Strauss, *Partial differential equations: An introduction*. John Wiley & Sons, 2007.
- [3] S. J. Farlow, *Partial differential equations for scientists and engineers*. Courier Corporation, 1993.
- [4] T. J. Hughes, *The finite element method: linear static and dynamic finite element analysis*. Courier Corporation, 2003.
- [5] R. J. LeVeque, *Finite difference methods for ordinary and partial differential equations: steady-state and time-dependent problems*. SIAM, 2007.
- [6] R. Hamming, *Numerical methods for scientists and engineers*. Courier Corporation, 2012.
- [7] B. Szabó and I. Babuška, “Finite element analysis: Method, verification and validation,” 2021.
- [8] W. Layton, *Introduction to the numerical analysis of incompressible viscous flows*. SIAM, 2008.

- [9] L. C. Berselli, T. Iliescu, and W. J. Layton, *Mathematics of large eddy simulation of turbulent flows*. Springer, 2006.
- [10] J. C. Strikwerda, *Finite difference schemes and partial differential equations*. SIAM, 2004.
- [11] S. L. Brunton and J. N. Kutz, “Promising directions of machine learning for partial differential equations,” *Nature Computational Science*, vol. 4, no. 7, pp. 483–494, 2024.
- [12] M. Raissi and G. E. Karniadakis, “Hidden physics models: Machine learning of nonlinear partial differential equations,” *Journal of Computational Physics*, vol. 357, pp. 125–141, 2018.
- [13] L. Lu, P. Jin, G. Pang, Z. Zhang, and G. E. Karniadakis, “Learning nonlinear operators via deepnet based on the universal approximation theorem of operators,” *Nature machine intelligence*, vol. 3, no. 3, pp. 218–229, 2021.
- [14] C. Mou, L. M. Smith, and N. Chen, “Combining stochastic parameterized reduced-order models with machine learning for data assimilation and uncertainty quantification with partial observations,” *Journal of Advances in Modeling Earth Systems*, vol. 15, no. 10, p. e2022MS003597, 2023.
- [15] E. Kharazmi, M. Cai, X. Zheng, Z. Zhang, G. Lin, and G. E. Karniadakis, “Identifiability and predictability of integer-and fractional-order epidemiological models using physics-informed neural networks,” *Nature Computational Science*, vol. 1, no. 11, pp. 744–753, 2021.
- [16] Y. Gu, J. Harlim, S. Liang, and H. Yang, “Stationary density estimation of itô diffusions using deep learning,” *SIAM Journal on Numerical Analysis*, vol. 61, no. 1, pp. 45–82, 2023.
- [17] Y. Teng, Z. Wang, L. Ju, A. Gruber, and G. Zhang, “Level set learning with pseudoreversible neural networks for nonlinear dimension reduction in function approximation,” *SIAM Journal on Scientific Computing*, vol. 45, no. 3, pp. A1148–A1171, 2023.
- [18] S. Manti, P.-H. Tsai, A. Lucantonio, and T. Iliescu, “Symbolic regression of data-driven reduced order model closures for under-resolved, convection-dominated flows,” *arXiv preprint arXiv:2502.04703*, 2025.
- [19] M. Raissi, P. Perdikaris, and G. E. Karniadakis, “Physics-informed neural networks: A deep learning framework for solving forward and inverse problems involving nonlinear partial differential equations,” *Journal of Computational Physics*, vol. 378, pp. 686–707, 2019.
- [20] S. Wang, S. Sankaran, and P. Perdikaris, “Respecting causality is all you need for training physics-informed neural networks,” *arXiv preprint arXiv:2203.07404*, 2022.
- [21] A. Krishnapriyan, A. Gholami, S. Zhe, R. Kirby, and M. W. Mahoney, “Characterizing possible failure modes in physics-informed neural networks,” *Advances in neural information processing systems*, vol. 34, pp. 26 548–26 560, 2021.
- [22] Z. Li, N. Kovachki, K. Azizzadenesheli, B. Liu, K. Bhattacharya, A. Stuart, and A. Anandkumar, “Fourier neural operator for parametric partial differential equations,” 2021.
- [23] N. B. Kovachki, S. Lanthaler, and H. Mhaskar, “Data complexity estimates for operator learning,” *arXiv preprint arXiv:2405.15992*, 2024.
- [24] S. Wang, H. Wang, and P. Perdikaris, “Learning the solution operator of parametric partial differential equations with physics-informed deepnets,” *Science advances*, vol. 7, no. 40, p. eabi8605, 2021.
- [25] B. Lu, C. Moya, and G. Lin, “Nsga-pinn: a multi-objective optimization method for physics-informed neural network training,” *Algorithms*, vol. 16, no. 4, p. 194, 2023.
- [26] B. Lu, C. Mou, and G. Lin, “Mopinnenkf: Iterative model inference using generic-pinn-based ensemble kalman filter,” *arXiv preprint arXiv:2506.00731*, 2025.
- [27] X. Ding and R. Ma, “Learning low-dimensional nonlinear structures from high-dimensional noisy data: An integral operator approach,” *The Annals of Statistics*, vol. 51, no. 4, pp. 1744–1769, 2023.
- [28] N. Winovich, M. Daneker, L. Lu, and G. Lin, “Active operator learning with predictive uncertainty quantification for partial differential equations,” *arXiv preprint arXiv:2503.03178*, 2025.
- [29] Z. Zou, X. Meng, A. F. Psaros, and G. E. Karniadakis, “Neuraluq: A comprehensive library for uncertainty quantification in neural differential equations and operators,” *SIAM Review*, vol. 66, no. 1, pp. 161–190, 2024.
- [30] K. Deb, A. Pratap, S. Agarwal, and T. Meyarivan, “A fast and elitist multiobjective genetic algorithm: Nsga-ii,” *IEEE transactions on evolutionary computation*, vol. 6, no. 2, pp. 182–197, 2002.
- [31] M. Welling and Y. W. Teh, “Bayesian learning via stochastic gradient langevin dynamics,” in *Proceedings of the 28th international conference on machine learning (ICML-11)*, 2011, pp. 681–688.

- [32] W. Deng, Q. Feng, L. Gao, F. Liang, and G. Lin, “Non-convex learning via replica exchange stochastic gradient mcmc,” in *International Conference on Machine Learning*. PMLR, 2020, pp. 2474–2483.
- [33] W. Deng, S. Liang, B. Hao, G. Lin, and F. Liang, “Interacting contour stochastic gradient langevin dynamics,” *arXiv preprint arXiv:2202.09867*, 2022.
- [34] H. Zheng, H. Du, Q. Feng, W. Deng, and G. Lin, “Constrained exploration via reflected replica exchange stochastic gradient langevin dynamics,” *arXiv preprint arXiv:2405.07839*, 2024.
- [35] T. Chen and H. Chen, “Universal approximation to nonlinear operators by neural networks with arbitrary activation functions and its application to dynamical systems,” *IEEE Transactions on Neural Networks*, vol. 6, no. 4, pp. 911–917, 1995.
- [36] Y. Tian, L. Si, X. Zhang, R. Cheng, C. He, K. C. Tan, and Y. Jin, “Evolutionary large-scale multi-objective optimization: A survey,” *ACM Computing Surveys (CSUR)*, vol. 54, no. 8, pp. 1–34, 2021.
- [37] W.-J. Hong, P. Yang, and K. Tang, “Evolutionary computation for large-scale multi-objective optimization: A decade of progresses,” *International Journal of Automation and Computing*, vol. 18, no. 2, pp. 155–169, 2021.
- [38] M. Li and X. Yao, “Quality evaluation of solution sets in multiobjective optimisation: A survey,” *ACM Computing Surveys (CSUR)*, vol. 52, no. 2, pp. 1–38, 2019.
- [39] N. Röckendorf, C. Nehls, and T. Gutschmann, “Design of membrane active peptides considering multi-objective optimization for biomedical application,” *Membranes*, vol. 12, no. 2, p. 180, 2022.
- [40] J. Park, S. Kang, S. Kim, H.-S. Cho, S. Heo, and J. H. Lee, “Techno-economic analysis of solar powered green hydrogen system based on multi-objective optimization of economics and productivity,” *Energy Conversion and Management*, vol. 299, p. 117823, 2024.
- [41] Y. Pan, B. Ma, Y. Zeng, J. Tang, B. Zeng, and Z. Ming, “An evolutionary framework for modelling unknown behaviours of other agents,” *IEEE Transactions on Emerging Topics in Computational Intelligence*, vol. 7, no. 4, pp. 1276–1289, 2022.
- [42] T. Wei, J. Liu, A. Gupta, P. S. Tan, and Y.-S. Ong, “Bayesian forward-inverse transfer for multiobjective optimization,” in *International Conference on Parallel Problem Solving from Nature*. Springer, 2024, pp. 135–152.
- [43] A. Singh, S. R. Jena, A. Gupta, and T. Thajudeen, “Multi-objective bayesian optimization for the retrieval of aggregated aerosol structures from microscopic images,” *Journal of Aerosol Science*, vol. 186, p. 106556, 2025.
- [44] K. Deb and H. Jain, “An evolutionary many-objective optimization algorithm using reference-point-based non-dominated sorting approach, part i: solving problems with box constraints,” *IEEE transactions on evolutionary computation*, vol. 18, no. 4, pp. 577–601, 2013.
- [45] Y. Hua, Y. Jin, K. Hao, and Y. Cao, “Generating multiple reference vectors for a class of many-objective optimization problems with degenerate pareto fronts,” *Complex & Intelligent Systems*, vol. 6, no. 2, pp. 275–285, 2020.
- [46] Q. Liu, Y. Jin, M. Heiderich, and T. Rodemann, “Adaptation of reference vectors for evolutionary many-objective optimization of problems with irregular pareto fronts,” in *2019 IEEE Congress on Evolutionary Computation (CEC)*. IEEE, 2019, pp. 1726–1733.
- [47] Z. Liang, W. Hou, X. Huang, and Z. Zhu, “Two new reference vector adaptation strategies for many-objective evolutionary algorithms,” *Information Sciences*, vol. 483, pp. 332–349, 2019.
- [48] H. Seada and K. Deb, “Effect of selection operator on nsga-iii in single, multi, and many-objective optimization,” in *2015 IEEE Congress on Evolutionary Computation (CEC)*. IEEE, 2015, pp. 2915–2922.
- [49] Y. Yuan, H. Xu, and B. Wang, “An improved nsga-iii procedure for evolutionary many-objective optimization,” in *Proceedings of the 2014 annual conference on genetic and evolutionary computation*, 2014, pp. 661–668.
- [50] L. R. Farias, A. J. Santos, and M. R. Nobre, “A non-dominated sorting evolutionary algorithm updating when required,” *arXiv preprint arXiv:2507.03864*, 2025.
- [51] W. Deng, Q. Feng, L. Gao, F. Liang, and G. Lin, “Non-Convex Learning via Replica Exchange Stochastic Gradient MCMC,” 2020.
- [52] M. Welling and Y. W. Teh, “Bayesian Learning via Stochastic Gradient Langevin Dynamics,” 2011, pp. 681–688.
- [53] P. Dupuis, Y. Liu, N. Plattner, and J. D. Doll, “On the Infinite Swapping Limit for Parallel Tempering,” *SIAM J. Multiscale Modeling & Simulation*, vol. 10, 2012.
- [54] J. Dong and X. T. Tong, “Spectral gap of replica exchange langevin diffusion on mixture distributions,” *arXiv preprint*, 2020.

- [55] L. Lu, X. Meng, Z. Mao, and G. E. Karniadakis, “Deepxde: A deep learning library for solving differential equations,” *SIAM Review*, vol. 63, no. 1, pp. 208–228, 2021.
- [56] L. Lu, R. Pestourie, W. Yao, Z. Wang, F. Verdugo, and S. G. Johnson, “Physics-informed neural networks with hard constraints for inverse design,” *SIAM Journal on Scientific Computing*, vol. 43, no. 6, pp. B1105–B1132, 2021.
- [57] C. Mou, B. Koc, O. San, L. G. Rebholz, and T. Iliescu, “Data-driven variational multiscale reduced order models,” *Computer Methods in Applied Mechanics and Engineering*, vol. 373, p. 113470, 2021.
- [58] Z. Liu, F. Liu, and F. Zeng, “An alternating direction implicit spectral method for solving two dimensional multi-term time fractional mixed diffusion and diffusion-wave equations,” *Applied Numerical Mathematics*, vol. 136, pp. 139–151, 2019.
- [59] R.-l. Du and Z.-z. Sun, “Temporal second-order difference methods for solving multi-term time fractional mixed diffusion and wave equations,” *Numerical Algorithms*, vol. 88, pp. 191–226, 2021.
- [60] B. Lu, Z.-p. Hao, C. Moya, and G. Lin, “Fpinn-deeponet: An operator learning framework for multi-term time-fractional mixed diffusion-wave equations,” *Journal of Computational Physics*, 538, 114184.
- [61] G. Cruz, B. Renczes, M. C. Runacres, and J. Decuyper, “State-space kolmogorov arnold networks for interpretable nonlinear system identification,” *IEEE Control Systems Letters*, 2025.
- [62] G. Lin, C. Mou, and J. Zhang, “Energy-dissipative evolutionary kolmogorov-arnold networks for complex pde systems,” *arXiv preprint arXiv:2503.01618*, 2025.
- [63] D. Qi and J.-G. Liu, “Data assimilation models for computing probability distributions of complex multiscale systems,” *arXiv preprint arXiv:2503.22949*, 2025.
- [64] K. Law, A. Stuart, and K. Zygalakis, “Data assimilation,” *Cham, Switzerland: Springer*, vol. 214, p. 52, 2015.
- [65] N. Chen and A. J. Majda, “Efficient nonlinear optimal smoothing and sampling algorithms for complex turbulent nonlinear dynamical systems with partial observations,” *Journal of Computational Physics*, vol. 410, p. 109381, 2020.
- [66] D. Durant, A. A. Popov, and R. Zanetti, “Updating gaussian mixture weights using posterior estimates,” *IEEE Transactions on Aerospace and Electronic Systems*, 2025.
- [67] X. Liu, X. Liu, T. Kaman, X. Lu, and G. Lin, “Statistical learning for nonlinear dynamical systems with applications to aircraft-uav collisions,” *Technometrics*, vol. 65, no. 4, pp. 564–578, 2023.
- [68] J. Wang, X. Liu, H.-W. Shen, and G. Lin, “Multi-resolution climate ensemble parameter analysis with nested parallel coordinates plots,” *IEEE transactions on visualization and computer graphics*, vol. 23, no. 1, pp. 81–90, 2016.
- [69] C. Mou, E. Merzari, O. San, and T. Iliescu, “An energy-based lengthscale for reduced order models of turbulent flows,” *Nuclear Engineering and Design*, vol. 412, p. 112454, 2023.
- [70] R. A. Heinonen and P. H. Diamond, “Turbulence model reduction by deep learning,” *Physical Review E*, vol. 101, no. 6, p. 061201, 2020.
- [71] X. Yang, M. Choi, G. Lin, and G. E. Karniadakis, “Adaptive anova decomposition of stochastic incompressible and compressible flows,” *Journal of Computational Physics*, vol. 231, no. 4, pp. 1587–1614, 2012.